Fuzzy Non-Uniform Sampling for Inverse Decision-Making Modeling to Tune Microwave Filters

Linwei Guo, Weihua Cao, *Senior Member, IEEE*,
Wenkai Hu, *Senior Member, IEEE*, Wentao Wu, *Member, IEEE*, and Min Wu, *Fellow, IEEE*

***Abstract*—Microwave filters (MFs) are indispensable in communication systems for selecting specific frequency signals. The tuning of MFs is a demanding and time-consuming task, which can be addressed by the inverse decision-making model (IDMM). However, two main challenges arise in the sampling process for IDMM, namely, low efficiency due to the large number of samples and poor adaptability in the presence of uncertain initial positions. To overcome these challenges, a fuzzy non-uniform sampling (FNUS) method is proposed leveraging the flexibility of fuzzy logic system. Specifically, an adaptive sampling framework based on a fuzzy logic system is presented to handle the uncertainty of initial positions. Under this framework, a non-uniform sampling approach is devised to collect fewer samples far from the target and more samples close to the target. Given the similarity and single-sided distribution of samples in the raw dataset oriented to modeling, the tailored enhancement strategies are designed to improve dataset quality. Fnially, the efficiency and adaptability of FNUS are demonstrated to be superior to the existing methods through simulations. Furthermore, the practicality of FNUS is validated by experiments on physical MFs.**

***Index Terms*—Adaptive sampling, data-driven modeling, inverse decision-making, microwave filters, non-uniform sampling.**

I. Introduction

Microwave filters (MFs) are key assets to select the signals in specific frequencies, and thus play an essential role in modern communication systems [1]. The frequency-selection characteristics of MFs are corrected to compensate for the design and manufacturing errors by adjusting geometric parameters (GPs) in tuning process. This process relies heavily on human expertise, which imposes a heavy toll on time and resource [2]. As a result, automatic tuning methods are rapidly developing propelled by the great demand of MFs.

This work was supported by the National Natural Science Foundation of China under Grant 61773354, the Natural Science Foundation of Hubei Province under Grant 2020CFA031, the 111 project under Grant B17040, and the Program of China Scholarship Council under Grant 202306410070. *(Corresponding Author: Weihua Cao)*

Linwei Guo, Weihua Cao, Wenkai Hu, and Min Wu are with the School of Automation, China University of Geosciences, Wuhan 430074, China, with the Hubei Key Laboratory of Advanced Control and Intelligent Automation for Complex Systems, Wuhan 430074, China, and also with the Engineering Research Center of Intelligent Technology for Geo-Exploration, Ministry of Education, Wuhan 430074, China (e-mail: mambaguo@cug.edu.cn; weihuacao@cug.edu.cn; wenkaihu@cug.edu.cn; wumin@cug.edu.cn).

Wentao Wu is with the Department of Aeronautical and Aviation Engineering, The Hong Kong Polytechnic University, Hong Kong 999077, China (email: wen-tao.wu@polyu.edu.hk).

A. State of the Art on Automatic Tuning

Tuning aims to find the feasible GPs (FGPs) corresponding to the specified filtering requirements. The existing methods can be categorized into two categories, namely, the forward evolution based tuning and the inverse decision-making based tuning, which are summarized as follows:

*1) **Forward evolution based tuning**:* This technique adjusts GPs incrementally to improve filtering performance. Typical forward evolution based tuning methods are developed with feature comparison [2], [3], space mapping [4], heuristic optimization [5], and reinforcement learning [6]. The feature comparison method extracts circuit features from the measured performance parameters, and adjusts GPs based on the difference of the actual and target features [2], [3]. The space mapping method obtains FGPs by mapping the optimized GPs between two parameter spaces, and the mapping relationship is iteratively corrected to make mapping accurate [4]. The heuristic optimization method optimizes GPs through swarm search to reach the satisfying performance [5]. The reinforcement learning method dynamically changes tuning strategy to guide the adjustment of GPs based on the current performance and historical action effects [6].

A common issue of the aforementioned methods lies in the requirements of massive iterations. Implementing these iterations on the actual MFs not only diminishes tuning efficiency, but may also damages to MFs. The surrogate model that maps GPs to filtering performance is used to perform iterations in place of MFs [5], [7]. A simulation model based on full-wave electromagnetic analysis can reflect the characteristics of MFs accurately, but require huge computational time [8]. In contrast, data-driven models computes filtering performance fast, but need to handle the high-dimension parameters and global complex nonlinear relations.

*2) **Inverse decision-making based tuning**:* Inverse decision-making deduces the FGPs according to the specific filtering requirement. It is more efficient than forward evolution as it does not need massive iterations [9]. The key of this approach is to establish an inverse decision-making model (IDMM) that maps filtering performance to GPs [10]. Unlike surrogate models, IDMM is more concerned with the mapping relationship in the vicinity of FGPs, alleviating the above challenges.

Due to the complex electro-mechanical coupling characteristics of MFs, it is hard to obtain the analytical function of

This article has been accepted for publication in IEEE Transactions on Fuzzy Systems. This is the author's version which has not been fully edited and content may change prior to final publication. Citation information: DOI 10.1109/TFUZZ.2025.3604594

the inverse mapping relationship. A feasible solution is the data-driven modeling approaches [10], [11]. These approaches mainly contain sampling and modeling steps. Among them, sampling plays a foundational and key role. The quality and distribution of the collected samples directly influence the accuracy of the model. The number of the collected samples impacts the efficiency of the whole tuning process. Since collecting data on MFs is effort extensive due to the cumbersome operation, sampling for building IDMM has received extensive attention and are discussed in the next subsection.

B. State of the Art on Sampling for building IDMM

It is the most common way to collect samples randomly with a uniform distribution in microwave modeling [12], [13]. This way implies that each sample in the space has an equal probability of being collected. However, each sample is of unequal value for inverse modeling. IDMM aims to find FGPs $\boldsymbol{x}^*$ corresponding to the satisfying performance. The local mapping around $\boldsymbol{x}^*$ is rather important than the other mapping. The samples close to $\boldsymbol{x}^*$ are more valuable for improve the accuracy of IDMM, while the samples far away from $\boldsymbol{x}^*$ are of little help. As dateset quality depends on the degree where samples represent the space of interest to models [14], uniform sampling results in an low-quality dataset where more samples are located far from $\boldsymbol{x}^*$ while fewer are near $\boldsymbol{x}^*$. This case is unavoidable unless the sample number is sufficiently large. Therefore, non-uniform sampling methods have been developed to collect more samples in the vicinity of FGPs.

A hybrid sampling approach initially performs uniform sampling across the global space, followed by a greedy sampling to collect more samples around the best GPs of the current dataset [15]. An iterative sampling method determines the location and number of sampling based on the model performance in the previous phase by interpolation, until the interpolation error is less than the threshold [16]. A Bayesian-inspired method evaluates the outcome probability of adding new samples in different spaces and selects the space with the highest probability as the sampling space [17]. A parallel local sampling strategy is designed based on Gaussian process, by which multiple local samples are generated in parallel around the predicted optimal solution [18].

The above methods [15]–[18] increased the proportion of high-quality samples in dataset by identifying the potential space. However, the determination of the potential space requires the analysis of an initial dataset. The initial dataset is also collected randomly or uniformly. It means that the poor quality of the initial dataset will lead to the inefficient sampling. Meanwhile, these sampling methods are hardly employed to the various initial GPs of MFs in tuning process. Due to the unknown FGPs and uncertain GPs, it is hard to set sampling range. Too small range may not contain FGPs and lead to a low-quality dataset, while the large range have to increase the number of samples and results in low efficiency.

C. Motivations and Contributions

IDMM has been demonstrated to be more efficient than the forward evolution based tuning methods [9]. For data-driven IDMM, the key to build them is sampling process. The existing sampling methods faces two challenges, namely, the low efficiency due to large sample number, and the poor adaptability in the presence to uncertain initial positions. To handle these challenges, fuzzy logic system (FLS) is introduced to enhance the non-uniformity and adaptability of sampling.

FLS is a rule-based inference framework that is particularly effective for modeling and decision-making under uncertainty [19], as demonstrated in various applications such as robotics, autonomous vehicles, and other complex systems [20], [21]. Leveraging fuzzy rule reasoning, FLS can adaptively approach unknown targets from uncertain initial conditions based on available information [22], making them well suited for sampling tasks in microwave filter tuning. By introducing FLS into the sampling strategy, the need to manually define a fixed sampling range can be eliminated. More importantly, the variable universe mechanism in FLS allows the dynamic adjustment of the decision domains [23], [24], enabling the sampling step-size to be continuously adapted according to the local sample quality or sensitivity. This mechanism contributes to the non-uniformity of the dataset by allocating larger steps in space far from the target and finer steps near high-interest space, thereby enhancing the non-uniform of the dataset.

In light of above motivations, an fuzzy non-uniform sampling (FNUS) method is proposed to build IDMM for tuning MFs. The main contributions are threefold: 1) A FLS-based sampling framework is presented to increase the adaptation across diverse individuals; 2) under this framework, a non-uniform sampling approach is devised to collect samples efficiently. This approach contains the experience-based evaluation of sample quality and quality-driven inference of sampling position; 3) the modeling-oriented enhancement strategies are designed to deal with the similarity and single-sided distribution of samples and improve the dataset quality.

The remainder of this paper is organized as follows: Section II formulates the sampling problem. Section III gives the details of FNUS. Section IV presents simulation and experiment analysis, followed by conclusions in Section V.

II. Problem formulation

This section describes the tuning process based on IDMM, the modeling process of IDMM, and the problem of sampling.

A. Tuning process based on IDMM

In Fig. 1, the depths of holes in the cavity of MFs are considered as GPs, denoted by $\boldsymbol{x} = [x_1, ..., x_m]$, where m is the number of holes. Due to the error in production, the initial GPs $\boldsymbol{x}_0$ is often within a certain range I_0 of the design value $\hat{\boldsymbol{x}}$ in the normal distribution. Given $\boldsymbol{x}_0$, filtering performance is measured by a vector network analyzer (VNA) in the form of scatter matrix (S-matrix). S-matrix is denoted as $\boldsymbol{s} = \{\boldsymbol{s}_{11}, \boldsymbol{s}_{21}\} \in \mathbb{C}^{N_\gamma \times 2}$, where N_γ represents the number of sampling frequency points. Parameters $\boldsymbol{s}_{11}$ and $\boldsymbol{s}_{21}$ stand for the reflection and transmission characteristics, denoted by

$$\boldsymbol{s}_{11} = \boldsymbol{a}_{11} + i\times\boldsymbol{b}_{11}, \boldsymbol{s}_{21} = \boldsymbol{a}_{21} + i\times\boldsymbol{b}_{21}, \tag{1}$$

where i is the imaginary unit. The amplitudes of $\boldsymbol{s}_{11}$ and $\boldsymbol{s}_{21}$ construct the amplitude-frequency response (AFR). AFR

This article has been accepted for publication in IEEE Transactions on Fuzzy Systems. This is the author's version which has not been fully edited and content may change prior to final publication. Citation information: DOI 10.1109/TFUZZ.2025.3604594

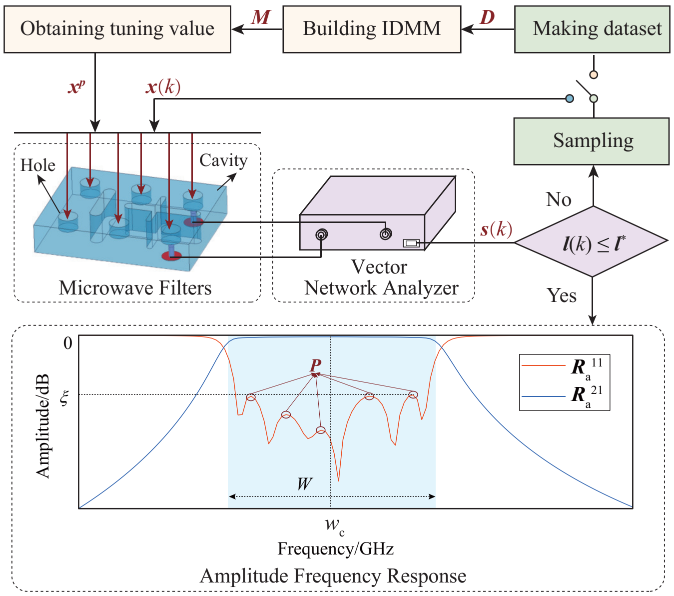

Fig. 1. The tuning process based on IDMM.

expresses the loss and gain of signal, denoted by $\boldsymbol{R}_a = \{\boldsymbol{R}_{11}^a, \boldsymbol{R}_{21}^a\} \in \mathbb{R}^{N_\gamma \times 2}$. $\boldsymbol{R}_{11}^a$ and $\boldsymbol{R}_{21}^a$ are calculated by

$$\begin{aligned} \boldsymbol{R}_{11}^a &= 20\log_{10}\sqrt{\boldsymbol{a}_{11}^2+\boldsymbol{b}_{11}^2}, \\ \boldsymbol{R}_{21}^a &= 20\log_{10}\sqrt{\boldsymbol{a}_{21}^2+\boldsymbol{b}_{21}^2}. \end{aligned} \tag{2}$$

AFR displays Performance indicators (PIs) intuitively, which are defined as follows:

1) Center frequency represents the center of passband and is calculated by

$$w_c = \sqrt{w_u * w_d}, \tag{3}$$

where w_u and w_d are the upper and down cut-off frequencies.

2) Bandwidth denotes the width of passband and is calculated by

$$W = w_u - w_d. \tag{4}$$

3) Return loss is the maximum amplitude of peaks $\boldsymbol{P}$ in the passband, namely,

$$\xi = \max\left(\mathcal{A}(\boldsymbol{P})\right), \tag{5}$$

where $\mathcal{A}(\cdot)$ calculates the amplitudes of peaks.

In the tuning process, center frequency and bandwidth are required to be within a certain range of the target values. This requirement means that the actual w_c and W that are too much greater or less than the target values will be unsatisfied. On the other hand, return loss should be below the target value. This requirement illustrates that the actual ξ is unsatisfied when it is greater than the target value and satisfied when less than the target value. In order to judge whether tuning is successful, differences of the actual and target PIs $\boldsymbol{d} = [d_1, d_2, d_3]$ are designed as

$$\begin{aligned} d_1 &= |(\sqrt{w_u \times w_d} - w_c^*)|, \\ d_2 &= |(w_u - w_d) - W^*)|, \\ d_3 &= \xi - \xi^*, \end{aligned} \tag{6}$$

where $|\cdot|$ represents the absolute operation; w_c^*, W^*, and ξ^* are the target PIs $\boldsymbol{P}^*$. The differences d_1 and d_2 reflect the accuracy of frequency selection. They are defined as absolute differences and thus do not take into account whether w_c and W are greater or less than the target values. The difference d_3 indicates the transmission quality. It is a signed value and defined as positive when the ξ is greater than ξ^*, negative when ξ is smaller than ξ^*, and zero when the two values are equal. Thus, MFs satisfy the requirements when

$$d_1 \le d_1^*,\ d_2 \le d_2^*,\ \text{and}\ d_3 \le d_3^*, \tag{7}$$

where $\boldsymbol{d}^* = [d_1^*, d_2^*, d_3^*]$ is the maximum allowable errors.

If the condition $\boldsymbol{d} \le \boldsymbol{d}^*$ is unsatisfying, GPs are tuned to $\boldsymbol{x}^p$, which is the predicted FGPs by IDMM $\boldsymbol{M}$.

B. Modeling process of IDMM

Data-driven IDMM is constructed through sampling and modeling. In the sampling step, $\boldsymbol{x}$ is adjusted and the corresponding $\boldsymbol{s}$ is measured after the adjustment. Each pair of $\boldsymbol{x}$ and $\boldsymbol{s}$ is considered as a sample, and all pairs constitute the dataset $\boldsymbol{D} = \{\boldsymbol{X}, \boldsymbol{S}\}$, where $\boldsymbol{X} = [\boldsymbol{x}(1), ..., \boldsymbol{x}(N_s)]^T$ and $\boldsymbol{S} = [\boldsymbol{s}(1), ..., \boldsymbol{s}(N_s)]^T$. In the modeling step, S-matrix is used as the input. With GPs as the output, IDMM is formulated as

$$\boldsymbol{x}^p = h(\boldsymbol{s}). \tag{8}$$

In this paper, the mapping relationship h is built using the state-of-art method in [25]. Once $\boldsymbol{M}$ is trained well, $\boldsymbol{x}^p$ is obtained by inputting the satisfying S-matrix $\boldsymbol{s}^*$ to $\boldsymbol{M}$.

In summary, tuning success rate depends on the accuracy of IDMM. When the modeling method is fixed, the accuracy is mainly affected by the dataset quality.

C. Sampling problem

Sample quality and sampling efficiency need to be considered simultaneously in the sampling process. To achieve the goals of high quality and efficiency, sampling is challenging not only caused by the unknown $\boldsymbol{x}^*$ and the uncertain $\boldsymbol{x}_0$, but the nonlinear mapping between GPs and PIs. Fig. 2 is an illustration that shows the complex sampling space. It can be seen from the left scatter-plots that the equally-spaced samples correspond to the uneven PIs, indicating the strong nonlinear. This nonlinear is more evident in the right heatmaps and intensifies with the increasing dimension of GPs. In addition, considering sampling efficiency, the number of samples in dataset is as small as possible while ensuring adequate characterization of the space that IDMM focuses on.

Based on the above discussion, sampling space is divided into the space B_a that is around $\boldsymbol{x}^*$ and the space B_f that is far from $\boldsymbol{x}^*$, i.e.,

$$\begin{aligned} B_a(\boldsymbol{x}^*) &= \{\boldsymbol{x} | \boldsymbol{d}(\boldsymbol{x}, \boldsymbol{x}^*) \le \boldsymbol{d}_s\}, \\ B_f(\boldsymbol{x}^*) &= \{\boldsymbol{x} | \boldsymbol{d}(\boldsymbol{x}, \boldsymbol{x}^*) > \boldsymbol{d}_s\}, \end{aligned} \tag{9}$$

where $\boldsymbol{d}_s$ is the boundary set of all dimensions that distinguishes the proximity of a sample to the target. The probability that a sample is collected in $B_a(\boldsymbol{x}^*)$ is

$$P_{B_a}(\boldsymbol{d}(\boldsymbol{x}, \boldsymbol{x}^*)) = \int_{B_a(\boldsymbol{x}^*)} p(\boldsymbol{x}|\boldsymbol{x}^*) d\boldsymbol{x}, \tag{10}$$

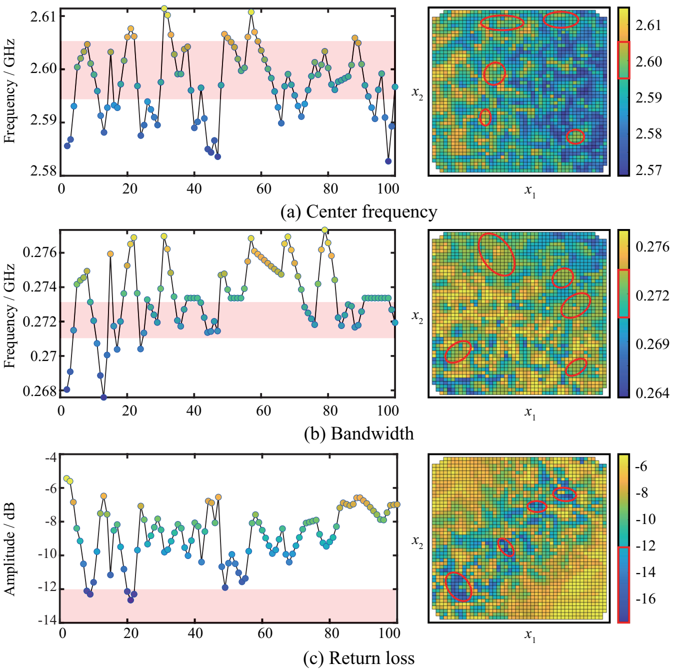

Fig. 2. The illustrative example of sampling space. Each sub-figure presents the variation of one performance indicator with two-dimensional GPs. The left scatter-plots display the indicators when x_1 is fixed and x_2 takes 100 samples at an equal interval within the boundaries of sampling range. The right heatmaps show PIs in the globe space. The unit of each color-bar in heatmap is the same with the unit of the vertical coordinate in the left scatter-plot. The targets of PIs are covered in red in the left scatter-plots, and boxed in red in the right color-bars. The spaces around the target PIs are circled in red in heatmaps.

where $p(\boldsymbol{x}|\boldsymbol{x}^*)$ represents the probability density function. The sampling object is to reduce N_s with $P_{B_a}(d(\boldsymbol{x},\boldsymbol{x}^*))$ as large as possible, namely,

$$\begin{aligned}&\textbf{min}\quad N_s \quad \textbf{s.t.}\\ &P_{B_a}(\boldsymbol{d}(\boldsymbol{x},\boldsymbol{x}^*))\geq \alpha_s,\\ &\boldsymbol{x}_0\sim\mathcal{N}(\hat{\boldsymbol{x}},\sigma^2)\quad \text{and}\quad \boldsymbol{x}_0\in[\hat{\boldsymbol{x}}-\boldsymbol{I}_0,\hat{\boldsymbol{x}}+\boldsymbol{I}_0],\\ &\boldsymbol{x}^* \text{ is unknown,}\end{aligned} \tag{11}$$

where $\mathcal{N}$ means normal distribution and σ is standard deviation; α_s is the desired probability of samples in $B_a(\boldsymbol{x}^*)$ relative to all samples; $\boldsymbol{I}_0$ is the set of possible variation ranges for GPs. To solve the problem, FNUS is designed.

III. Fuzzy non-uniform sampling

This section describes the framework of FNUS, and then gives the details of every part.

A. Framework of FNUS

Fig. 3 presents the framework of FNUS, which consists three parts, namely, the inference of sampling position, the evaluation of sample quality, and the enhancement of dataset.

To improve sampling fitness, GPs are adjusted one by one until the switch condition is met, other than adjusted simultaneously. Adjusting all GPs in turn once is called a round. In the new round $\sigma+1$, re-adjustment is conducted from x_1 to x_m until the completed condition is met.

The switching condition is that the maximum adjusting number N_a on a geometric parameter (GP) is reached, or the changes of evaluation results $\Delta F_g^{\sigma}(j-1)$ and $\Delta F_g^{\sigma}(j)$ are both less than a threshold θ_F, i.e.,

$$C_1=\begin{cases}1,\ \Delta F_{\sigma}^{g}(j-1)<\theta_F \text{ and } \Delta F_{\sigma}^{g}(j)<\theta_F \text{ or } \ j=N_a,\\ 0,\ \text{otherwise,}\end{cases} \tag{12}$$

where j is the adjusting number on x_g in the σth round, and $g=1,...,m$. The switching condition is performed when $j\geq 3$. The completed condition is that PIs reach the set value, i.e.,

$$C_2=\begin{cases}1,\ d_1\leq d_1^*,\ d_2\leq d_2^*,\ \text{and } d_3\leq\gamma\cdot d_3^*,\\ 0,\text{otherwise,}\end{cases} \tag{13}$$

where $\gamma\in[0,1]$ stands for the proximity to d_3^*. γ is set through experiments based on the fact that a larger γ improves the quality of the best sample but wastes more time.

In each adjusting, x_g^{σ} is calculated by

$$x_g^{\sigma}(j)=x_g^{\sigma}(0)+\sum_{j=1}^{J}u_g^{\sigma}(j), \tag{14}$$

where J is the total tuning number on x_g in the σth round. After each adjusting, $\boldsymbol{s}_{\sigma}^{g}(j)$ is measured by VNA, and the data pair $\{\boldsymbol{x}_{\sigma}^{g}(j),\boldsymbol{s}_{\sigma}^{g}(j)\}$ is obtained. All data pairs until the completed condition is met form the raw dataset $\boldsymbol{D}_0$={$\boldsymbol{X}_0,\boldsymbol{S}_0$}.

Subsequently, the enhancement strategies are conducted to improve dataset quality by removing similar samples from $\boldsymbol{D}_0$ to generate $\boldsymbol{D}_1$, and collecting high-quality samples around the final sample in $\boldsymbol{D}_1$ to obtain $\boldsymbol{D}_2$. Finally, the dataset $\boldsymbol{D}$ is constructed by combining the two sub-datasets $\boldsymbol{D}_1$ and $\boldsymbol{D}_2$.

B. Experience-based evaluation of sample quality

The evaluation of sample quality guides the inference of sampling position and judges whether sampling is completed. Since the boundary $\boldsymbol{d}_s$ is hard to determine, expert experience is introduced. Manual tuning goes through the frequency and loss adjustment stages successively. In the frequency adjustment (FA) stage, w_c and W are adjusted in large increments, while ξ is fine-tuned in smaller steps under the satisfying w_c^* and W^* during the loss adjustment (LA) stage. Consequently, samples from the FA stage are considered to be far from $\boldsymbol{x}^*$ and of lower quality, whereas samples from the LA stage are viewed as closer to $\boldsymbol{x}^*$ and of higher quality.

According to subsection II.A, there are three direct PIs. In addition, the number of peaks n_R reflects the state of resonators. Specifically, n_R equals to $m-1$ if all resonators are in good state. It is also an important reference for evaluation and taken as another indicator. If these four PIs are the inputs of FLS, the computational complexity would get increased dramatically [26]. Therefore, the comprehensive evaluation for multiple PIs is designed, where PIs are categorized into two groups based on their importance at different stages, namely,

$$F(j)=\boldsymbol{\alpha}_f(j)\left[\bar{f}_1(j)+\bar{f}_2(j),\bar{f}_3(j)+\bar{f}_4(j)\right]^T, \tag{15}$$

where $F(j)$ is the evaluation result of the jth sampling; sub-functions $\bar{f}_1(j)$-$\bar{f}_4(j)$ are the normalized results of four PIs to avoid the influences of different units and variable ranges; $\boldsymbol{\alpha}_f(j)$ is the weight vector of sub-functions. The sample quality is evaluated after each sampling, so the scripts σ and g are omitted in this sub-section.

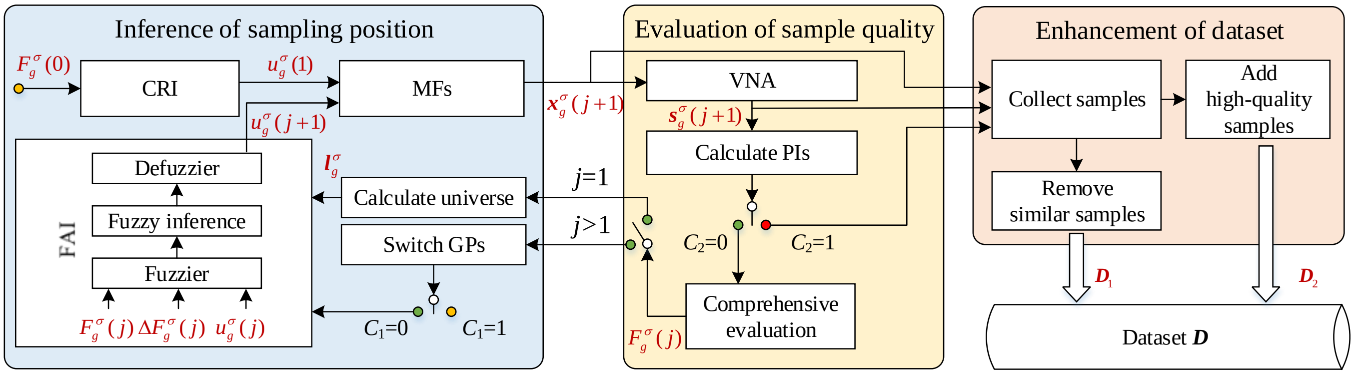

Fig. 3. The framework of FNUS.

1) Normalized sub-functions: The first three sub-functions are related to differences d_1, d_2, and d_3, respectively. They are defined as

$$\bar{f}_q = \max(1 - 2/(1 + e^{\beta_q * d_q}), 0), q = 1, 2, 3, \quad (16)$$

where β_q is an expansion-factor that make $\bar{f}_q$ vary obviously within their respective ranges, and is determined by experiments. The sub-function $\bar{f}_4$ relates to n_R, and is defined as

$$\bar{f}_4 = [(m-1) - n_R]/(m-1). \quad (17)$$

All sub-functions belong to $[0, 1)$ and with the same monotonicity, i.e., a lower value indicates higher quality.

2) Weight vector: The vector $\boldsymbol{\alpha}_f$ emphases the corresponding sub-functions in different stages, and is defined as

$$\boldsymbol{\alpha}_f = \begin{cases} \left[\alpha_f^1, 1\right], & \bar{f}_1 > \bar{f}_1^* \text{ and } \bar{f}_2 > \bar{f}_2^* \text{ (FA stage)}, \\ \left[1, \alpha_f^2\right], & \text{otherwise(LA stage)}, \end{cases} \quad (18)$$

where $\alpha_f^1 > \alpha_f^2 > 1$; $\bar{f}_1^*$ and $\bar{f}_2^*$ are calculated by

$$\bar{f}_q^* = 1 - 2/(1 + e^{\beta_q * d_q^*}), q = 1, 2. \quad (19)$$

C. Quality-driven inference of sampling position

The inference of sampling position consists of constrained random inference (CRI) and fuzzy adaptive inference (FAI). They both adjust sampling step-sizes driven by sample quality.

For the first sampling on $\boldsymbol{x}_g^\sigma$, CRI is performed by

$$u_g^\sigma(1) = \begin{cases} \max(r_1 \cdot \boldsymbol{I}_0(g) * F_g^\sigma(0)/\tilde{F}, \theta_x), r_1 \geq 0 \\ \min(r_1 \cdot \boldsymbol{I}_0(g) * F_g^\sigma(0)/\tilde{F}, -\theta_x), r_1 < 0 \end{cases} \quad (20)$$

where r_1 is a random number in $[-1, 1]$ to increase sample diversity, which is enhanced by setting the minimum adjusting value $\theta_x \in \mathbb{R}^+$; $F_g^\sigma(0)$ represents the evaluation result of $\boldsymbol{s}_g^\sigma(0)$; $\tilde{F}$ denotes the maximum of all evaluations so far, which is used to normalize $F_g^\sigma(0)$.

The following sampling positions on $\boldsymbol{x}_g^\sigma$ are calculated by FAI. The inputs of FAI include the current evaluation $F(j)$, the change of evaluation $\Delta F(j) = F(j) - F(j-1)$, and the current change of sampling position $u(j)$. The output of FAI is the next change of sampling position $u(j+1)$.

The key of fuzzy logic dealing with uncertain is fuzzy sets and rules. To construct fuzzy sets, the inputs and output of FAI are fuzzified by the membership functions shown in Fig. 3. The fuzzy set of $F(j)$ consists of small (S), middle (M), and big (B), which stands for good, medium, and poor quality, respectively. The fuzzy set of $\Delta F(j)$ is composed of negative big (NB), negative small (NS), positive small (PS), and positive big (PB). They reflect the changing trend of performance that is better dramatically, better slightly, worse slightly, and worse dramatically, respectively. The fuzzy sets of $u(j)$ and $u(j+1)$ are NB, NS, PS, and PB, indicating the adjusting direction and range that is reverse large, reverse small, forward small, and forward large, respectively.

To achieve non-uniform sampling, the universe set $\boldsymbol{l} = \{l_F, l_{\Delta F}, l_u\}$ is dynamically changed. The universe boundary of $F(j)$ is determined based on the range of F, i.e., $l_F = 2 * \alpha_f^1 + 2$ in the FA stage and $l_F = 2 * \alpha_f^2 + 2$ in the LA stage. The universes of $u(j)$ and $u(j+1)$ are changed for each GP in every round because it plays a direct role in referring sampling position. The universe l_u is calculated by

$$l_u = F_\sigma^g(0) \cdot e^{-\mathrm{sgn}[\bar{\lambda}(\sigma,g) - \Phi(\bar{\boldsymbol{\lambda}})]\bar{\lambda}(\sigma,g)} \cdot \boldsymbol{I}_0(g), \quad (21)$$

where $\bar{\lambda}(\sigma, g)$ is the normalized sensitivity and the initial sensitivity $\lambda(\sigma, g) = |\Delta F_\sigma^g(1)|/u_\sigma^g(1)$; $\bar{\boldsymbol{\lambda}}$ stands for the normalized $\boldsymbol{\lambda}$ using the max-min normalization, and $\boldsymbol{\lambda}$ is the sensitivity sequence containing all $\lambda(\sigma, g)$; $\Phi(\bar{\boldsymbol{\lambda}})$ indicates the median of $\bar{\boldsymbol{\lambda}}$; the operator sgn[·] is defined as

$$\mathrm{sgn}[\bar{\lambda}(\sigma,g) - \Phi(\bar{\boldsymbol{\lambda}})] = \begin{cases} 1, \bar{\lambda}(\sigma,g) > \Phi(\bar{\boldsymbol{\lambda}}) \\ 0, \bar{\lambda}(\sigma,g) = \Phi(\bar{\boldsymbol{\lambda}}) \\ -1, \bar{\lambda}(\sigma,g) < \Phi(\bar{\boldsymbol{\lambda}}), \end{cases} \quad (22)$$

According to Eqn. (21), l_u is influenced by the initial sample quality $F_\sigma^g(0)$ and the sensitivity $\bar{\lambda}(\sigma, g)$ in the vicinity of the initial sample. A high $F_\sigma^g(0)$ indicates the low quality, resulting in a large universe boundary, vice versa. For $\bar{\lambda}(\sigma, g)$, it is compared with $\Phi(\bar{\boldsymbol{\lambda}})$ to dynamically evaluate sensitivity. When $\bar{\lambda}(\sigma, g)$ is high, l_u is compressed for the accurate exploitation. Otherwise, l_u is expanded for the wide exploration. With the constant membership function, a large l_u leads to larger steps and fewer samples, enhancing global exploration. In contrast, a small l_u leads to smaller steps and more samples, improving local exploitation around $\boldsymbol{x}^*$.

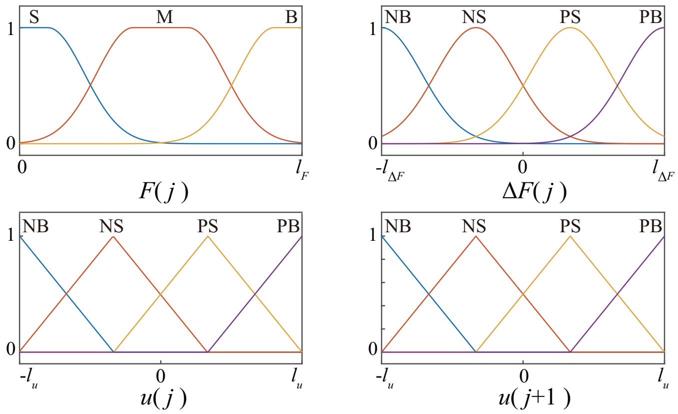

Fig. 4. The membership functions of inputs and output.

TABLE I
FUZZY RULES OF AFI

$F(k)$	$u(k)$ \ $\Delta F(k)$	NB	NS	PS	PB
B	NB	NB	NB	PB	PB
	NS	NS	NB	PB	PB
	PS	PS	PB	NB	NB
	PB	PB	PB	NB	NB
M	NB	NS	NB	PB	PB
	NS	NS	NS	PS	PB
	PS	PS	PS	NS	NB
	PB	PS	PB	NB	NB
S	NB	NS	PB	PS	PS
	NS	NS	NS	PS	PS
	PS	PS	PS	NS	NS
	PB	PS	PB	NS	NS

Fuzzy rules are in the "IF-THEN" form [27], and listed in TABLE I. The design principles are as follows.

1) When $F(j)$ is big, the aim of AFI is to collect fewer samples and enter into the LA stage quickly in the FA stage; when in the LA stage, samples converge closer to the $\boldsymbol{x}^*$. The strategy of changing sampling position tends to be bold.

2) When $F(j)$ is middle, sampling may be in a phase shift from FA to LA, or in the neighbor of $\boldsymbol{x}^*$. The strategy of changing sampling position is suggested to be conservative relatively. Unless when quality gets much worse, a substantial reverse changing is necessary.

3) When $F(j)$ is small, sampling is most in the LA stage and AFI is expected to collect more samples. The strategy of changing sampling position is conservative.

D. Modeling-oriented enhancement of dataset

The raw dataset $\boldsymbol{D}_0$ has two shortcomings that affect dataset quality for building IDMM. Firstly, there are massive samples with similar responses caused by GPs with minor differences. As shown in Fig. 5(a), each group (1-3, 4-7, 8-12, and 16-18) contains multiple samples, and the responses $\boldsymbol{R}_a^{11}$ are

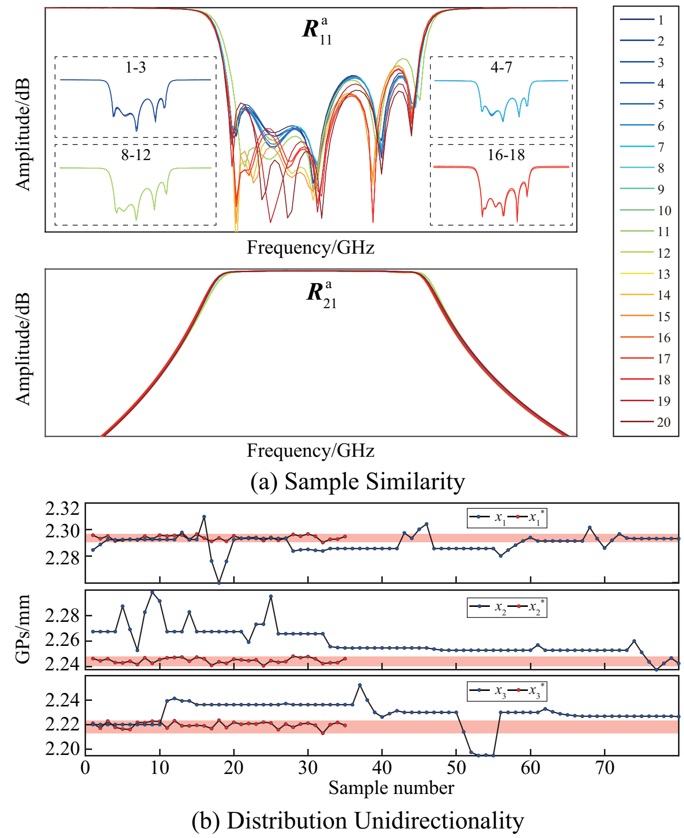

Fig. 5. Analysis of samples in $\boldsymbol{D}_0$. Sub-figure (a) shows $\boldsymbol{R}_{11}^a$ and $\boldsymbol{R}_{21}^a$ of 20 samples continuously collected using CRI and FAI. The amplitude-frequency response $\boldsymbol{R}_{21}^a$ is similar for almost all samples. Moreover, the amplitude-frequency response $\boldsymbol{R}_{11}^a$ also shows that there are some similar groups, such as numbers 1-3, 4-7, 8-12, and 16-18. These observations confirm the existence of sample similarity in the raw dataset. Sub-figure (b) shows the locations of some FGPs (x_1^*, x_2^*, and x_3^*) and GPs of samples in $\boldsymbol{D}_0$ (x_1, x_2, and x_3). The red ranges are the boundaries of FGPs.

almost overlapping with each other. These samples increase the risk of overfitting when modeling and rise the time of training IDMM. This case often happens especially in the LA stage, due to the fact that the changing of sampling position becomes progressively smaller with the decreasing of F. Notably, the proximity of GPs is a necessary but not sufficient condition for similar responses. In the high-sensitivity space of GPs, small changes of GPs lead to the obvious changes of responses, mainly in return loss. Thus, the removal of similar samples should consider the distances on GPs and return loss simultaneously.

Secondly, samples are usually concentrated on one side of $\boldsymbol{x}^*$, as shown in Fig. 5(b). The goal of FAI is to approach $\boldsymbol{x}^*$ quickly, so FAI does not explore the global space widely, but rather sampling in a certain direction. Thus, almost all samples are above or below $\boldsymbol{x}^*$. This leads to the sampling space uncovering $\boldsymbol{x}^*$ or the underdevelopment of the neighborhood of $\boldsymbol{x}^*$. These two shortcomings are addressed by the following ways for a high-quality dataset.

1) The removal of similar samples based on double distances (DD-SSR): It can be seen that the double distances are prioritized differently, i.e., the distance of GPs is considered before the distance of return loss. Thus, the removal of similar

Algorithm 1 DD-SSR

Input: Sorted sub-dataset $\vec{\boldsymbol{D}}_\sigma^g$;
Output: Sub-dataset $\tilde{\boldsymbol{D}}_\sigma^g$ that removed similar samples;

$\tilde{\boldsymbol{D}}_\sigma^g$=$\vec{D}_\sigma^g(1)$;
for n = 1 to $N_\sigma^g - 1$ **do**
  $d_x = |\vec{\boldsymbol{x}}_\sigma^g(n+1) - \tilde{\boldsymbol{x}}_\sigma^g(\text{end})|$;
  if $d_x \geq \theta_x$ **do**
    $\tilde{\boldsymbol{D}}_\sigma^g$=[$\tilde{\boldsymbol{D}}_\sigma^g$;$\vec{D}_\sigma^g(n+1)$];
  else do
    $d_\xi = \vec{\boldsymbol{\xi}}_\sigma^g(n+1) - \tilde{\boldsymbol{\xi}}_\sigma^g(end)$;
    if $|d_\xi| \geq \theta_\xi$ **do**
      $\tilde{\boldsymbol{D}}_\sigma^g$=[$\tilde{\boldsymbol{D}}_\sigma^g$;$\vec{D}_\sigma^g(n+1)$];
    else
      if $d_\xi < 0$ **do**
        $\tilde{D}_\sigma^g$(end)=$\vec{D}_\sigma^g(n+1)$;
      end if
    end if
  end if
end for

samples considers the distances of GPs firstly. Additionally, the complexity of calculating distances among all samples is very high. Due to the sampling characteristic of one by one, the whole dataset is segmented into several parts according to the switching of GPs. For the sub-dataset $\boldsymbol{D}_g^\sigma$, all samples are obtained from the sampling process on x_g in the σth round. They are sorted in the ascending order based on x_g first. Then, the DD-SSR is designed.

For the sorted sub-dataset $\vec{\boldsymbol{D}}_\sigma^g$, the distances between neighboring samples d_x are calculated. If d_x is less than the threshold θ_x, the distances of ξ are considered. If d_x is still less than the threshold θ_ξ, two neighboring samples are diagnosed as similar. Then, the later of the two samples is removed and the earlier sample continues to be compared with the next one. Finally, all the sub-datasets make up the dataset $\boldsymbol{D_1} = \{\boldsymbol{X_1}, \boldsymbol{S_1}\}$. This algorithm is summarized in Algorithm 1, where N_σ^g represents the sample number of $\vec{\boldsymbol{D}}_\sigma^g$; $\vec{D}_\sigma^g(1)$ is the first sample in $\vec{\boldsymbol{D}}_\sigma^g$; $\boldsymbol{x}_\sigma^g$ and $\boldsymbol{\xi}_\sigma^g$ contains the GPs and return loss of all samples in $\boldsymbol{D}_g^\sigma$, respectively.

2) The adding of high-quality samples using minimum distance rejection (MDR-HQSA): Although most samples concentrated on one side of $\boldsymbol{x}^*$, they are close to $\boldsymbol{x}^*$, especially the final sample. Thus, uniform sampling in the vicinity of the final sample in $\boldsymbol{D}_1$ increases the exploitation to the neighborhood of $\boldsymbol{x}^*$, and declines the risk of uncovering $\boldsymbol{x}^*$. Specially, N_s^2 samples are collected by uniform sampling with minimum distance rejection in a small range [15], i.e.,

$$\boldsymbol{x} = \boldsymbol{D}_1(\text{end}) + \boldsymbol{r}_2, \tag{23}$$

where $\boldsymbol{D}_1(\text{end})$ is the final sample in $\boldsymbol{D}_1$; $\boldsymbol{r}_2 \in \mathbb{R}^{1*m}$ is a random vector, and each element in $\boldsymbol{r}_2$ belongs to the range $(-\boldsymbol{\phi}_{r_2}, -\theta_x) \cup (\theta_x, \boldsymbol{\phi}_{r_2})$, where $\boldsymbol{\phi}_{r_2} \in \mathbb{R}^+$ is the sampling boundary and determined by experiments. These samples construct the dataset $\boldsymbol{D_2} = \{\boldsymbol{X_2}, \boldsymbol{S_2}\}$. Notably, similar samples in $\boldsymbol{D}_2$ are avoided by the mechanism of minimum distance rejection. Additionally, similar samples between $\boldsymbol{D}_1$ and $\boldsymbol{D}_2$ are few because samples in $\boldsymbol{D}_1$ are almost linearly arranged but in $\boldsymbol{D}_2$ are evenly distributed in high-dimensional space.

Finally, the dataset $\boldsymbol{D}$ used for training IDMM is comprised of $\boldsymbol{D_1}$ and $\boldsymbol{D_2}$.

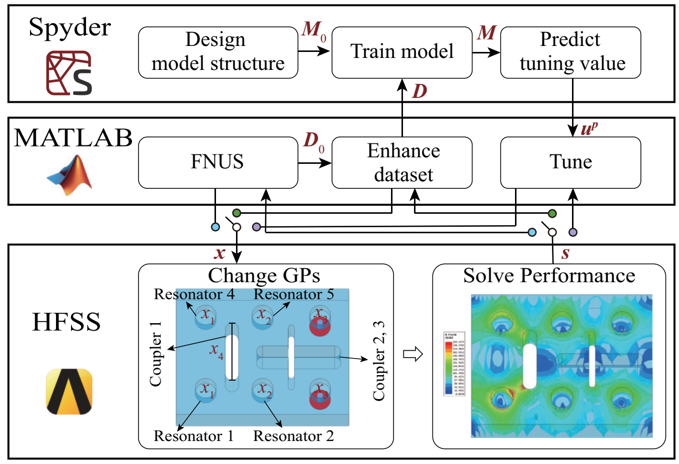

Fig. 6. The scheme of the simulation platform.

IV. Case Studies

In this section, the effectiveness and advantages of the proposed FNUS are demonstrated on simulations by comparing with the state-of-the-art sampling methods, and the practicality of FNUS is validated by experiments on physical MFs.

A. Simulation set-up

The simulation platform was built based on HFSS, MATLAB and Spyder. HFSS is a 3D electromagnetic simulation software that widely used in the design and analysis of MFs. It was utilized for solving S-matrix. MATLAB was used for performing FNUS and constructing dataset. In Spyder, IDMM was built and the predicting FGPs were obtained.

The simulated microwave filter in Fig. 6 integrates six resonators arranged in a symmetrical structure. Coupling between resonators is achieved through a crossing coupler and a lateral coupler. In order to focus on the validation of the proposed FNUS, the depths of resonators were initially selected as the tuning variables in simulations. Due to the symmetrical structure, the output of IDMM was defined as $\boldsymbol{x} = [x_1, x_2, x_3]$, and each GP varies in the range ± 0.03 mm. This setup allows for a focused comparison of the effects of different sampling methods on building IDMM while ensuring the fundamental tuning conditions. Additionally, the target PIs were $w_c^* = 2.6083$GHz, $W^* = 0.193$GHz, and $\xi^* = -20$dB. The maximum allowable values were $d_1^* = 0.002$GHz, $d_2^* = 0.001$GHz, and $d_3^* = 0$.

The parameters of FNUS were detailed below. The weights of sub-functions were $\alpha_f^1 = 5$ and $\alpha_f^1 = 3$. The expansion-factors were $\beta_1 = 300$, $\beta_2 = 1000$, and $\beta_3 = 0.2$. The thresholds were $\theta_x = 0.0005$ mm and $\theta_\xi = 0.02$. The parameters of switching condition were $N_a = 5$ and $\theta_F = 0.0001$. The parameter of completed condition γ and the sampling range and number of MDR-HQSA were determined in simulations.

This article has been accepted for publication in IEEE Transactions on Fuzzy Systems. This is the author's version which has not been fully edited and content may change prior to final publication. Citation information: DOI 10.1109/TFUZZ.2025.3604594

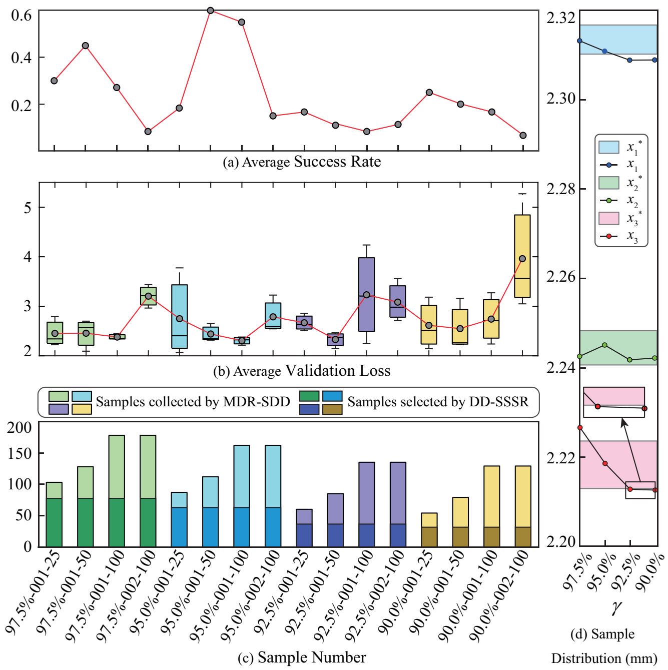

Fig. 7. Results of parameter analysis. Sub-figure (a) shows the average tuning success rate of training IDMM three times using the dataset obtained by each parameter group. Sub-figure (b) shows the box plots of the validation error and presents the average validation errors in the dotted line. Sub-figure (c) displays the sample numbers of FNUS with different parameter group. The above three sub-figures share the same horizontal coordinate, which displays the different parameter groups and is named as "γ-sampling range-sampling number". Sub-figure (d) exhibits the locations of the final samples in all datasets dealt by DD-SSSR, where the colored regions are covered by twenty $\boldsymbol{x}^*$.

In all below simulations, IDMM was built using the modeling method in [25]. The validation error is calculated using mean absolute deviation (MAD), denoted as

$$L = \kappa_L \frac{1}{N_v} \sum\nolimits_{q=1}^{N_v} \left| \boldsymbol{x}_q^p - \boldsymbol{x}_q^* \right|, \tag{24}$$

where $\kappa_L = 1000$ is a factor to make L more obvious and avoid gradient disappearance; N_v is the sample number of validation set; $\boldsymbol{x}_q^p$ represents the predicted value obtained by inputting the qth sample in validation set, where $\boldsymbol{x}_q^*$ is the actual value.

B. Parameter analysis

Proximity γ is a key parameter that determines the end of FNUS, which also affects the subsequent MDR-HQSA in terms of sampling range and number. These parameters were determined by comparative analysis. Specially, four different values of γ (97.5%, 95%, 92.5%, and 90%) were set. For each γ, two sampling ranges (± 0.01 mm and ± 0.02 mm) and three sample numbers (25, 50, and 100) were set. All sampling in this subsection was based on the same initial GPs. Each dataset was used to train IDMM for three times, and each IDMM was tested by twenty kinds of $\boldsymbol{x}^*$. The sample quality was reflected by the tuning results and validation errors of IDMM, which are shown below.

In sub-figure 7(a), the average success rates under $\gamma = 97.5\%$ and $\gamma = 95\%$ are more than those under $\gamma = 92.5\%$ and $\gamma = 90\%$. The result is due to two reasons. One is that there are more samples in $\boldsymbol{D}_1$ to characterize the sampling space covering the initial and final sampling samples when γ is bigger, as shown in sub figure 7(c). The other one is that the final sample in $\boldsymbol{D}_1$ is closer to $\boldsymbol{x}^*$ for big γ, as shown in sub figure 7(d), which provides a good base for MDR-HQSA. Additionally, a small γ may cause the final sample in $\boldsymbol{D}_1$ being located in some spurious local optimum rather than in a real region close to $\boldsymbol{x}^*$. Therefore, a big γ is suggested.

The results when $\gamma = 97.5\%$ and $\gamma = 95\%$ are compared in sub-figures 7(a) and (b). The datasets collecting 50 samples in the range ± 0.01mm by MDR-HQSA achieve the maximum average success rates and the smaller validation error variance, which strike balance in $\boldsymbol{D}_1$ and $\boldsymbol{D}_2$. Since the final sample in $\boldsymbol{D}_1$ is close to $\boldsymbol{x}^*$, a larger sampling range is unnecessary; otherwise, a large number of samples would have to be collected. In a small range, if the sample number of $\boldsymbol{D}_2$ is small, $\boldsymbol{D}$ has insufficient representation of the vicinity of $\boldsymbol{x}^*$. Finally, the parameter group is chosen as $\gamma = 95\%$, $\boldsymbol{\phi}_{r_2} = 0.01$ mm, and $N_s^2 = 50$, because it gets the higher success rate with fewer samples compared to the group "97.5%-001-50".

TABLE II
SAMPLING EFFICIENCY COMPARISON RESULTS OF DIFFERENT METHODS.

Sampling method	FNUS	MCS				HS			
		0.02		0.04		30%		70%	
N_s	131	200	400	200	400	200	400	200	400
$\bar{n}_c$	12	0.33	5	5.33	9.33	2.67	3	7.33	10.33
ψ	0.85	0.02	0.12	0.25	0.23	0.13	0.07	0.35	0.25

C. Efficiency analysis

Sampling efficiency means the speed of collecting samples that can build an accurate IDMM, which is inversely related to the sample number, and associated with the modeling accuracy. Here, it was defined as

$$\psi = \bar{n}_c / (1 + \kappa_\psi * N_s), \tag{25}$$

where $\bar{n}_c$ was the average number of successful tuning and stood for modeling accuracy; N_s denoted the sample number; κ_ψ was a factor to make ψ more obvious and $\kappa_\psi = 0.1$ was used as the default value.

The sampling efficiency of FNUS was compared with other two state-of-the-art sampling methods. One is Monte Carlo sampling (MCS), which is the representative uniform sampling method that collects a fixed number of samples in a pre-set range in uniform distribution (MCS has been implemented practically in [5], [25], [28]). The other one is hybrid sampling (HS) that combines local and globe sampling; it belongs to the non-uniform sampling based on the initial dataset (HS has been implemented practically in [15]). The range of MCS was set to ± 0.02mm and ± 0.04mm. To verify the impact of the initial dataset on sample quality, HS was based on two initial datasets $\boldsymbol{D}_0^1$ and $\boldsymbol{D}_0^2$. The ratios υ_h of high-quality samples to all samples in these two initial datasets were 30% and 70%. Additionally, both MCS and HS methods were used to make

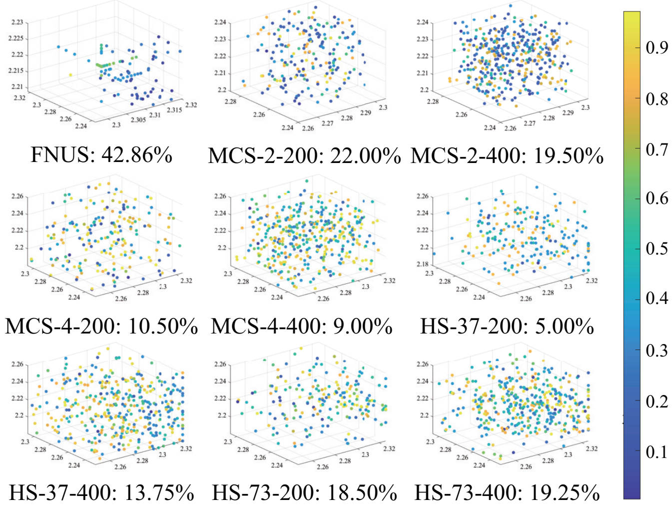

Fig. 8. Distributions of samples collected by all comparative methods. The color of each sample represents the normalized $\bar{F}$, referring to the right color-bar. Three axes denote GPs in millimeters. The naming rule is “method name, sampling range/the rate of the initial dataset, sampling name” except for FNUS. Then, the name of every method is followed by υ_h.

two datasets with 200 and 400 samples. Each set of simulation was based on the same initial GPs. Each dataset was used to train IDMM for three times, and each IDMM was used to repeat tuning MFs for 20 times. The tuning results are presented in TABLE II.

For FNUS, although the samples used to train IDMM were $\boldsymbol{D}_1$ and $\boldsymbol{D}_2$, the sample number used to calculate sampling efficiency was set to the sum of N_s^0 and N_s^2. Even so, N_s of FNUS is minimal among all methods. In addition, the IDMM trained with the FNUS-collected samples successfully tuned MFs the most times. Accordingly, FNUS achieves the highest efficiency compared to other representative methods. For MCS, the small sampling range (± 0.02mm) and the range covered by twenty FGPs overlap only a small portion. A small number of samples cannot characterize the area covered by FGPs well, resulting in a low-accuracy IDMM. Notwithstanding more samples increase the accuracy of IDMM, but the effect is constrained. A large sampling range can cover all FGPs, but a lot of samples is necessary. For HS, even though a high-quality initial dataset can improve the quality of the whole dataset obviously, this initial dataset is hard to obtain. Likewise, when using HS, more samples are required to get a high-accuracy IDMM when in a large range.

To analyze why the sampling efficiency of FNUS is high, the sample distribution of all methods are presented in Fig. 8. The evaluation result of performance F is normalized to [0,1] by max-min normalization, namely,

$$\bar{F} = (F - F_{\min})/(F_{\max} - F_{\min}), \tag{26}$$

where $F_{\max} = 12$ and $F_{\min} = 0$. The rate υ_h is low using MCS, demonstrating that the uniform distribution of samples over the GP space results in non-uniform space of performance. The rate υ_h using MCS with ± 0.02mm sampling range is twice the rate υ_h with ± 0.04mm, illustrating FGPs only locate in a small range. The rate υ_h using HS is affected by the initial dataset strongly, and a high-quality initial dataset can cause a high υ_h. Additionally, the rate υ_h would be improved with the increasing N_s. This is caused by the mechanism that local sampling around the current optimal sample. When the sampling number is large, the current optimal sample is closer to $\boldsymbol{x}^*$ and more high-quality samples are collected. Compared to other methods, the rate υ_h of FNUS is highest (42.86%), as it reduces the low-quality samples and focuses on collecting high-quality samples. In fact, the non-uniform characteristic of dataset is increased due to FAI and MDR-HQSA. Fig. 9 shows the adjustment values u of GP calculated by FNUS. It converges to 0 gradually, indicating the FNUS explores sampling space widely in the FA stage while exploits space elaborately in the LA stage. Therefore, the FNUS effectively improves the sample quality and sampling efficiency.

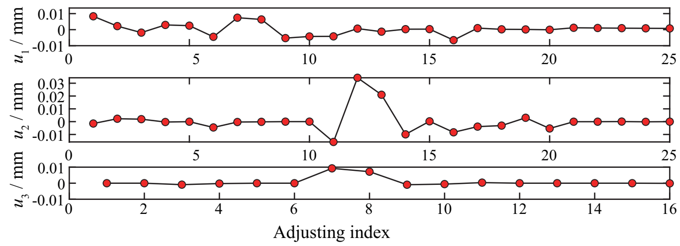

Fig. 9. The adjustment of sampling positions calculated by two kinds of inference.

D. Adaptation analysis

The adaptability refers to the correlation between the sample quality and the parameter setting of sampling methods when oriented to MFs with various initial GPs. Sample quality is reflected by $\bar{n}_c$, and strong correlation means poor adaptability.

To simulate the errors in the actual production, five kinds of initial GPs were generated randomly around the neighborhood of the design GPs in normal distribution. The PIs of MFs with differrnt initial GPs are presented in TABLE III. For the analysis of adaptation, FNUS is compared with MCS due to the fact that MCS and HS are both affected by the sampling range. FNUS keeps the same parameter setting as before. The difference in the parameter setting of MCS were mainly in two sampling ranges, with sampling number set based on the principle of consistency in sample density. Likewise, twenty replicate testing were performed in each set of simulation. The results are presented in TABLE III.

The numbers $\bar{n}_c$ always maintain at a high level when using the FNUS on the various initial GPs with the same parameter setting. However, the MCS method with varying sampling ranges exhibits significant performance differences when faced with the different initial GPs. Besides, the FNUS collected fewer samples but achieved a higher number of successful tuning compared to the MCS across two parameter settings, regardless of the initial GPs. Consequently, the FNUS is adaptive.

To analyze how FNUS adapts to various initial GPs, the distribution of $\boldsymbol{x}_0$ and D_1(end) in five simulations are presented in Fig. 10. The distances of all $\boldsymbol{x}_0$ from $\boldsymbol{x}^*$ are indeterminate and at least one dimension is far away from $\boldsymbol{x}^*$, while all

TABLE III
SAMPLING ADAPTATION RESULTS OF DIFFERENT METHODS ON MFS WITH DIFFERENT INITIAL GPS

Sampling methods			FNUS					MCS	
								±0.02mm	±0.04mm
Sample number N_s			131	99	96	193	119	200	400
MFs with the different initial GPs	Index	PIs	Average success number $\bar{n}_c$						
	1	w_c=2.6141GHz, W=0.193GHz, ξ=-6.535dB	12.00	\	\	\	\	0.33(11.67 ↓)	9.33(2.67 ↓)
	2	w_c=2.6163GHz, W=0.193GHz, ξ=-15.21dB	\	10.67	\	\	\	5(5.67 ↓)	5.33(5.33 ↓)
	3	w_c=2.5943GHz, W=0.189GHz, ξ=-13.17dB	\	\	10.67	\	\	3.33(7.33 ↓)	4.67(6.00 ↓)
	4	w_c=2.6042GHz, W=0.193GHz, ξ=-6.38dB	\	\	\	10.33	\	1(9.33 ↓)	3(7.33 ↓)
	5	w_c=2.5962GHz, W=0.193GHz, ξ=-15.15dB	\	\	\	\	11.33	3.33(8.00 ↓)	4.00(7.33 ↓)

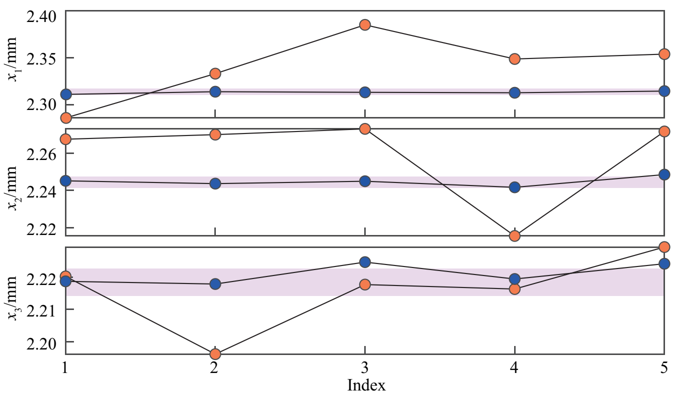

Fig. 10. The distributions of $\boldsymbol{x}_0$ and $\widehat{\boldsymbol{x}}$. The orange points represents $\boldsymbol{x}_0$, and the blue points stand for $\widehat{\boldsymbol{x}}$. The purple ranges cover all $\boldsymbol{x}^*$.

D_1(end) are in or very close to the space covered by $\boldsymbol{x}^*$. This indicates that FNUS gradually approaches from the uncertain $\boldsymbol{x}_0$ to the vicinity of the unknown $\boldsymbol{x}^*$, by which the parameter setting problem can be resolved so that MDR-HQSA is always performed in a small space to obtain high-quality samples.

E. Validation on MFs with both adjustable resonance and coupling parameters

The above simulations have demonstrated the higher efficiency and better adaptation of FNUS than the existing representative sampling methods on MFs with only adjustable resonance parameters. In order to simulate more complex and representative tuning scenarios, coupling parameters are also taken into account in this subsection. Coupling parameters are related to the energy transfer between resonators. As presented in Fig. 6, Coupler 1 is near to Resonators 1, 2, 4 and 5, enabling significant adjustment of the coupling strength between these resonators. In contrast to Couplers 2 and 3, the position and size of Coupler 1 can be independently controlled without breaking the overall geometrical symmetry. Therefore, the width of Coupler 1 was chosen as the coupling parameter to be adjusted, denoted as x_4. The output of IDMM was defined as $\boldsymbol{x} = [x_1, x_2, x_3, x_4]$, with the variation range of x_4 is $\pm 0.5mm$.

The validation of FNUS on MFs with both adjustable resonance and coupling parameters was conducted with the comparison to MCS. The initial values of all GPs were set randomly in $\boldsymbol{I}_0$. For the dateset enhancement stage of the FNUS method, the sampling ranges of x_1, x_2, and x_3 were $\pm 0.01mm$ and that of x_4 was $\pm 0.05mm$; the sampling number was 50, 100, respectively. For the MCS method, the sampling ranges of x_1, x_2, and x_3 were $\pm 0.03mm$ and that of x_4 was $\pm 0.5mm$; the sampling number was set to 500, 700, 900, and 1100, respectively. Every set of simulation was performed five times and each simulation used twenty S-matrices that meet the requirements for test. Then, the average value of the successful tuning numbers was calculated to enhance the reliability of results. The comparison results are presented in TABLE IV, where the sampling number of the FNUS method used the number before removing similarity and $\kappa_\psi = 0.02$. The sampling efficiency of the proposed FNUS is very high because it collects fewer samples but builds IDMMs with the larger $\bar{n}_c$ compared to MCS. As the sampling number raised, the sampling efficiency of FNUS gradually increased but that of MCS decreased. This is because few samples collected in the dataset enhancement stage of FNUS were all close to the target and of high quality, whereas many samples obtained through MCS were dispersed across the entire sampling space, with only a small portion exhibiting high quality.

TABLE IV
COMPARISON RESULTS OF FNUS AND MCS ON MFS WITH BOTH ADJUSTABLE RESONATOR AND COUPLING PARAMETERS.

Sampling method	FNUS		MCS			
N_s	353	403	500	700	900	1100
$\bar{n}_c$	5.8	7.6	2.4	3.4	4	4.8
ψ	0.720	0.839	0.218	0.227	0.211	0.209

Fig. 11 illustrates the tuning performance of IDMMs built by tow sampling methods for the same $\boldsymbol{s}^*$. It can be seen that the IDMM built by FNUS (IDMM-FUNS) yields better performance than the IDMM built by MCS (IDMM-MCS). This is because FNUS collected more high-quality samples around the target, which provides more detailed features to IDMM. In conclusion, the effectiveness of FNUS is verified on MFs with both adjustable resonance and coupling parameters.

This article has been accepted for publication in IEEE Transactions on Fuzzy Systems. This is the author's version which has not been fully edited and
content may change prior to final publication. Citation information: DOI 10.1109/TFUZZ.2025.3604594

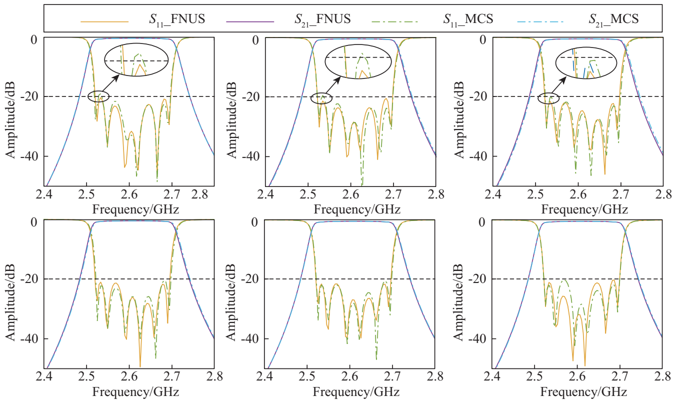

Fig. 11. The tuning performance of IDMMs built by FNUS and MCS on the MF with both adjustable resonance and coupling parameters, where N_s of MCS was 1100.

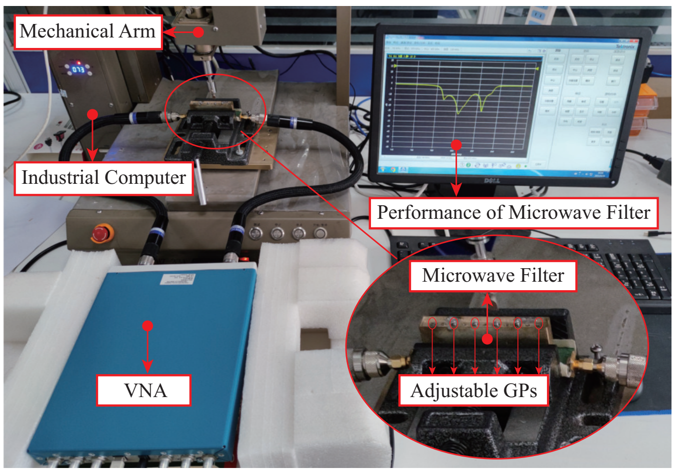

Fig. 12. The actual tuning platform. It contains the physical MF, a VNA for measuring the performance of MF, a mechanical arm for adjusting GPs, and an industrial computer for computing the adjusting values through the proposed method, as well as showing the measured performance.

F. Experiment validation on the physical MF

To validate the effectiveness of the proposed FNUS method in the practical tuning scenario, both FNUS and MCS were applied on a physical MF, as shown in Fig. 12 [28]. The MF is equipped with six adjustable GPs. Due to manufacturing errors, the actual values of these GPs deviated from the designed ones by unknown amounts, resulting in a detuned MF with an initial S11 measured at –6.71 dB, as illustrated in Fig. 13. Therefore, this experiment represents a typical tuning case.

The target PIs of the physical MF were $w_c^* = 0.805$GHz, $W^* = 0.04$GHz, and $\xi^* = -15$dB. The maximum allowable differences were $d_1^* = 0.002$GHz, $d_2^* = 0.001$GHz, and $d_3^* = 0$. To tune this physical MF, IDMMs were constructed with the output $\boldsymbol{x} = [x_1, x_2, x_3, x_4, x_5, x_6]$ based on two sampling methods. For MDR-HQSA of FNUS, the sampling range of each GP was set to [-18°, 18°], with a total of 100 samples collected. For MCS, the sampling range was set to [-135°, 135°], with sampling numbers set to 437, 655, and 874, respectively. As in the previous simulations, the

TABLE V
COMPARISON RESULTS OF FNUS AND MCS ON THE PHYSICAL MF.

Sampling method	FNUS	MCS		
N_s	437	437	437*1.5	437*2
$\bar{n}_c$	8.4	4.4	5.6	6.0
ψ	0.862	0.419	0.367	0.300

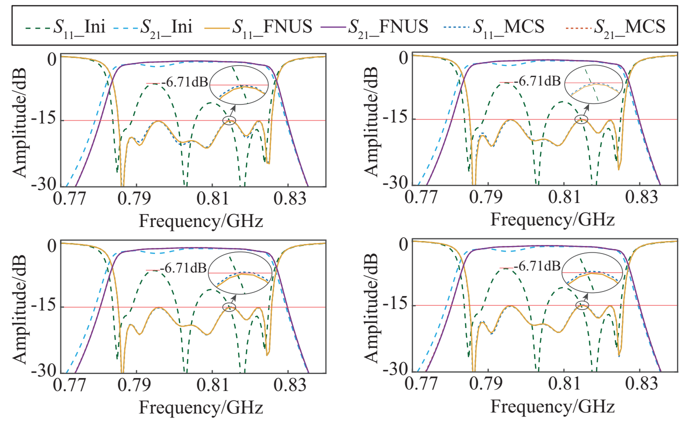

Fig. 13. The tuning performance of IDMMs obtained by FNUS and MCS on the physical MF, where N_s of MCS was 874. The legends "S_{11}_Ini" and "S_{21}_Ini" represent the pre-tuning performance, "S_{11}_FNUS" and "S_{21}_FNUS" stand for the post-tuning performance by IDMM-FNUS, and "S_{11}_MCS" and "S_{21}_MCS" are the post-tuning performance by IDMM-MCS.

samples collected by all methods were used to construct IDMMs through the same modeling approach described in [25]. Subsequently, the same set of S-matrices were put into each IDMM to obtain the corresponding adjusted value of each GP.

The tuning results are summarized in Table V. Using the proposed FNUS method, 437 samples were collected and used to train five models. Each model was evaluated on tuning tasks, and achieved an average of 8.4 successful tuning outcomes. In contrast, IDMMM-MCS achieved only 4.4 successful tuning outcomes with 437 samples, and merely 6 successful tuning outcomes even when the sample size was increased to two times. Fig. 13 illustrates the tuning results derived from the IDMMs built using both methods. The tuning results obtained using two IDMMs were generally similar and closely approximate the target performance, indicating that both models were capable of capturing coarse-grained features from the performance responses. However, the return loss could meet the specified requirement with a higher probability when using IDMM-FNUS compared to IDMM-MCS. This indicates that IDMM-FNUS demonstrates superior capability in extracting fine-grained features. This advantage arises from the dual strengths of FNUS in adaptive exploration and precise exploitation. It is capable of efficiently navigating from an uncertain initial state to the vicinity of the target, where it gathers a large number of high-quality samples to support accurate modeling.

To comprehensively validate the effectiveness and robustness of FNUS, it was compared to MCS on a large number

TABLE VI
SAMPLING ADAPTATION RESULTS OF DIFFERENT METHODS ON THE PHYSICAL MF WITH DIFFERENT INITIAL GPS

Sampling methods		FNUS					MCS	
							±90°	±135°
Sample number N_s		437	433	472	373	555	655	874
	PIs	Average success number $\bar{n}_c$						
MFs with the different initial GPs	ξ=-6.71dB	8.4	\	\	\	\	4.4	6
	ξ=-6.52dB	\	10.2	\	\	\	5.6	8.8
	ξ=-5.67dB	\	\	9	\	\	4.4	7.8
	ξ=-6.89dB	\	\	\	8.2	\	3.6	7.6
	ξ=-6.37dB	\	\	\	\	9.2	4.2	8

of sampling experiments starting from different initial GPs. In these experiments, FNUS maintained a set of parameter settings, while MCS had different sets of parameter settings. The return losses corresponding to five kinds of initial points were generally poor, so the experiments were representative. As in the previous experiments, each dataset was used to train the model five times, and the same set of S-matrices was applied for testing. The average numbers of successful tunings $\bar{n}_c$ for all datasets are summarized in TABLE VI.

Across all five initial GPs, FNUS consistently achieves a higher average number of successful tunings than MCS, while using fewer or comparable samples. Specifically, with a similar number of samples, FNUS obtains better results, demonstrating that the samples it collects are of higher quality and more informative for modeling. Even when MCS collects nearly twice as many samples, its numbers of successful tunings approach that of FNUS. These clearly confirm that FNUS is more efficient and provides higher tuning accuracy, thereby validating its effectiveness. In addition, FNUS also shows stable performance across different initial GPs. In contrast, MCS is highly sensitive to both the sampling range and the initial GPs, leading to larger fluctuations in $\bar{n}_c$ (from 3.6 to 8.8). This indicates that FNUS is less dependent on parameter setting and initial GPs, thereby exhibiting stronger robustness in practical tuning scenarios.

In summary, the proposed FNUS method demonstrates a strong capability to efficiently collect high-quality samples under uncertain initial GPs. This enables the construction of a more accurate IDMM with significantly lower sampling cost, thereby validating the practical effectiveness of FNUS in real-world tuning applications.

V. CONCLUSION

This paper presents an adaptive and efficient fuzzy non-uniform sampling method for building IDMM to tune MFs with individual difference. By introducing FLS, the proposed method effectively addresses the challenges posed by uncertain initial positions. The designed CRI and FAI mechanisms enable non-uniform data acquisition by dynamically adjusting the sampling step-size based on sample quality and local sensitivity, resulting in more high-quality samples and fewer low-quality ones. Additionally, the dataset quality is further improved through enhancement strategies that solve the shortcomings of similarity and single-sided distribution of samples. The simulation results illustrated that FNUS had a higher sampling efficiency compared to either the uniform sampling method or the non-uniform sampling methods. Meanwhile, FNUS showed greater adaptability to MFs with various initial GPs, compared to sampling methods that require more settings. Furthermore, physical experiments further confirm its practical applicability in real-world tuning tasks.

Importantly, this study showcases a novel application of FLS in the design of sampling strategies. By leveraging the uncertainty-handling capability of FLS, FNUS adaptively selects informative samples, without relying on large-scale data or predefined sampling distribution. Accordingly, FNUS holds substantial potential for the applicability expansion into various fields where existing the similar sampling problem. Therefore, extending FNUS to broader domains is a valuable research direction. Additionally, leveraging the collected samples to construct accurate IDMMs is worthwhile.

REFERENCES

[1] A. Liu, Y. Wu, M. Leng, Y. Zeng, and M. Yu, “Adaptive homotopy-based inverse model for the geometry scaling of microwave filters,” *IEEE Transactions on Microwave Theory and Techniques*, vol. 72, no. 1, pp. 680–695, Jan. 2024.

[2] H. Huang, F. Feng, S. Huang, L. Chen, and Z. Hao, “Microscale searching algorithm for coupling matrix optimization of automated microwave filter tuning,” *IEEE Transactions on Cybernetics*, vol. 53, no. 5, pp. 2829–2840, May 2023.

[3] C. Kwak, M. Uhm, I. Yom, and H. J. Eom, “Automated microwave filter tuning using curve similarity and weighted least squares,” *IEEE Microwave and Wireless Components Letters*, vol. 22, no. 10, pp. 539–541, Oct. 2012.

[4] J. C. Melgarejo, J. Ossorio, S. Cogollos, M. Guglielmi, V. E. Boria, and J. W. Bandler, “On space mapping techniques for microwave filter tuning,” *IEEE Transactions on Microwave Theory and Techniques*, vol. 67, no. 12, pp. 4860–4870, Dec. 2019.

[5] L. Bi, W. Cao, W. Hu, and M. Wu, “Intelligent tuning of microwave cavity filters using granular multi-swarm particle swarm optimization,” *IEEE Transactions on Industrial Electronics*, vol. 68, no. 12, pp. 12 901–12 911, Dec. 2021.

[6] Z. Wang, Y. Ou, X. Wu, and W. Feng, “Continuous reinforcement learning with knowledge-inspired reward shaping for autonomous cavity filter tuning,” in *2018 IEEE International Conference on Cyborg and Bionic Systems (CBS)*, Oct. 2018, pp. 53–58.

[7] Y. Yu, Z. Zhang, Q. S. Cheng, B. Liu, Y. Wang, C. Guo, and T. T. Ye, “State-of-the-art: Ai-assisted surrogate modeling and optimization for microwave filters,” *IEEE Transactions on Microwave Theory and Techniques*, vol. 70, no. 11, pp. 4635–4651, Nov. 2022.

[8] Y. Zhou, J. Xie, Q. Ren, H. H. Zhang, and Q. H. Liu, “Fast multi-physics simulation of microwave filters via deep hybrid neural network,” *IEEE Transactions on Antennas and Propagation*, vol. 70, no. 7, pp. 5165–5178, Jul. 2022.

[9] L. Bi, W. Cao, Y. Shi, W. Hu, L. Guo, and M. Wu, “Dynamic hybrid models with active sampling and adaptive selection of double-domain features for the tuning of microwave cavity filters,” *IEEE Transactions on Cybernetics*, vol. 54, no. 8, pp. 4828–4840, Aug. 2024.

[10] Y. Wu, G. Pan, D. Lu, and M. Yu, “Artificial neural network for dimensionality reduction and its application to microwave filters inverse modeling,” *IEEE Transactions on Microwave Theory and Techniques*, vol. 70, no. 11, pp. 4683–4693, Nov. 2022.

[11] C. Yu, Q. Li, F. Feng, and Q.-J. Zhang, “Convolutional neural network with adaptive batch-size training technique for high-dimensional inverse modeling of microwave filters,” *IEEE Microwave and Wireless Technology Letters*, vol. 33, no. 2, pp. 122–125, Feb. 2023.

[12] J. Jin, C. Zhang, F. Feng, W. Na, J. Ma, and Q.-J. Zhang, “Deep neural network technique for high-dimensional microwave modeling and applications to parameter extraction of microwave filters,” *IEEE Transactions on Microwave Theory and Techniques*, vol. 67, no. 10, pp. 4140–4155, Oct. 2019.

[13] C. Zhang, J. Jin, W. Na, Q.-J. Zhang, and M. Yu, "Multivalued neural network inverse modeling and applications to microwave filters," *IEEE Transactions on Microwave Theory and Techniques*, vol. 66, no. 8, pp. 3781–3797, Aug. 2018.

[14] M. Javaheripi, M. Samragh, T. Javidi, and F. Koushanfar, "Adans: Adaptive non-uniform sampling for automated design of compact dnns," *IEEE Journal of Selected Topics in Signal Processing*, vol. 14, no. 4, pp. 750–764, May 2020.

[15] Z. Zhang, Q. S. Cheng, H. Chen, and F. Jiang, "An efficient hybrid sampling method for neural network-based microwave component modeling and optimization," *IEEE Microwave and Wireless Components Letters*, vol. 30, no. 7, pp. 625–628, Jul. 2020.

[16] Q.-J. Zhang, E. Gad, B. Nouri, W. Na, and M. Nakhla, "Simulation and automated modeling of microwave circuits: State-of-the-art and emerging trends," *IEEE Journal of Microwaves*, vol. 1, no. 1, pp. 494–507, Jan. 2021.

[17] Z. Zhou, Z. Wei, J. Ren, Y.-X. Sun, Y. Yin, G. F. Pedersen, and M. Shen, "Bayesian-inspired sampling for efficient machine-learning-assisted microwave component design," *IEEE Transactions on Microwave Theory and Techniques*, vol. 72, no. 2, pp. 996–1007, Feb. 2024.

[18] W. Na, K. Liu, H. Cai, W. Zhang, H. Xie, and D. Jin, "Efficient em optimization exploiting parallel local sampling strategy and bayesian optimization for microwave applications," *IEEE Microwave and Wireless Components Letters*, vol. 31, no. 10, pp. 1103–1106, Oct. 2021.

[19] L. Bi, W. Cao, W. Hu, and M. Wu, "A dynamic-attention-based heuristic fuzzy expert system for the tuning of microwave cavity filters," *IEEE Transactions on Fuzzy Systems*, vol. 30, no. 9, pp. 3695–3707, Sep. 2022.

[20] C. Dong, Z. Yu, X. Chen, H. Chen, Y. Huang, and Q. Huang, "Adaptability control towards complex ground based on fuzzy logic for humanoid robots," *IEEE Transactions on Fuzzy Systems*, vol. 30, no. 6, pp. 1574–1584, Jun. 2022.

[21] W. Wu, Y. Zhang, Z. Jia, J.-G. Lu, and W. Zhang, "Adaptive fault-tolerant fuzzy containment control for networked autonomous surface vehicles: A noncooperative game approach," *IEEE Transactions on Fuzzy Systems*, vol. 32, no. 7, pp. 4192–4204, Jul. 2024.

[22] Y. Jiang, Z. Peng, D. Wang, Y. Yin, and Q.-L. Han, "Cooperative target enclosing of ring-networked underactuated autonomous surface vehicles based on data-driven fuzzy predictors and extended state observers," *IEEE Transactions on Fuzzy Systems*, vol. 30, no. 7, pp. 2515–2528, Jul. 2022.

[23] Y. Jin, W. Cao, M. Wu, and Y. Yuan, "Data-based variable universe adaptive fuzzy controller with self-tuning parameters," *Applied Soft Computing*, vol. 123, p. 108944, Jul. 2022.

[24] M. Wang, C. Yang, W. Wang, Z. Lu, L. Yang, and R. Chen, "An efficient power control scheme for heavy-duty hybrid electric vehicle with online optimized variable universe fuzzy system," *IEEE Transactions on Fuzzy Systems*, vol. 32, no. 5, pp. 2725–2737, May 2024.

[25] L. Guo, W. Cao, L. Bi, W. Hu, Y. Yuan, and M. Wu, "A dynamic tuning decision-making model using multi-feature fusion," *IEEE Transactions on Circuits and Systems II: Express Briefs*, vol. 70, no. 2, pp. 601–605, Feb. 2023.

[26] C. Li, J. Gao, J. Yi, and G. Zhang, "Analysis and design of functionally weighted single-input-rule-modules connected fuzzy inference systems," *IEEE Transactions on Fuzzy Systems*, vol. 26, no. 1, pp. 56–71, Feb. 2018.

[27] Mamdani, "Application of fuzzy logic to approximate reasoning using linguistic synthesis," *IEEE Transactions on Computers*, vol. C-26, no. 12, pp. 1182–1191, Dec. 1977.

[28] L. Guo, W. Cao, L. Bi, W. Hu, and M. Wu, "Knowledge-driven dynamic multi-objective evaluation and attention optimization for tuning microwave filters," *Applied Soft Computing*, vol. 171, p. 112702, 2025.

Linwei Guo received the B.S. degree in automation, in 2020, from the China University of Geosciences, Wuhan, China, where he is currently working toward the Ph.D. degree in control science and engineering.

From February 2024 to February 2025, he was a Visiting Research Scholar at the Department of Mechanical Engineering, University of Victoria, BC, Canada. His research interests include intelligent control, data-driven modeling, and knowledge-driven optimization for complex systems.

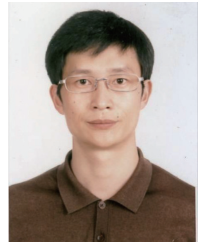

Weihua Cao (Senior Member, IEEE) received his B.S., M.S., and Ph.D. degrees in Engineering from Central South University, Changsha, China, in 1994, 1997, and 2007, respectively.

He was a faculty member of the School of Information Science and Engineering at Central South University from 1997 to 2014, and was promoted to Professor in 2009. In 2014, he joined the China University of Geosciences, Wuhan, China, where he is a professor in the School of Automation. He was a visiting student with Kanazawa University Ishikawa, Japan, from 1996 to 1997, and a visiting scholar with the Department of Electrical Engineering, Alberta University, Edmonton, AB, Canada, from 2007 to 2008. His research interests include perception and modeling in complex environments, intelligent robotics and equipment, and process control.

Wenkai Hu (Senior Member, IEEE) received the B.Eng. and M.Sc. degrees in Power and Mechanical Engineering from Wuhan University, Wuhan, China, in 2010 and 2012, respectively, and the Ph.D. degree in Electrical and Computer Engineering from the University of Alberta in 2016. After that, he was with the Dept. of Electrical & Computer Engineering in the University of Alberta as a Post-Doctoral Fellow from Oct. 2016 to Sep. 2018 and a Research Associate from Nov. 2018 to Feb. 2019. He is currently a Professor with China University of Geosciences, Wuhan, China. His research interests include advanced alarm monitoring, process control, and data mining for complex industrial processes.

Wentao Wu (Member, IEEE) received the B.S. degree from Harbin University of Science and Technology, Harbin, China, in 2018, the M.S. degree from Dalian Maritime University, Dalian, China, in 2021, and the Ph.D. degree in electronic information engineering from Shanghai Jiao Tong University, Shanghai, China.

From January to November 2024, he was a Visiting Research Scholar at the Department of Mechanical Engineering, University of Victoria, BC, Canada. Currently, he is a Postdoctoral Fellow in the Department of Aeronautical and Aviation Engineering, The Hong Kong Polytechnic University. His current research interests include distributed control, safety-critical control, game theory, and their applications in autonomous systems.

Dr. WU was selected for the inaugural Doctoral Special Program of Young Elite Scientist Sponsorship Program by China Association for Science and Technology (CAST) in 2025. He is a Youth Editorial Board Member of Journal of Artificial Intelligence & Control Systems. He serves as a reviewer of many international journals.

Min Wu (Fellow, IEEE) received his B.S. and M.S. degrees in engineering from Central South University, Changsha, China, in 1983 and 1986, respectively, and his Ph.D. degree in engineering from the Tokyo Institute of Technology, Tokyo, Japan, in 1999.

He was a faculty member of the School of Information Science and Engineering at Central South University from 1986 to 2014, and was promoted to Professor in 1994. In 2014, he joined the China University of Geosciences, Wuhan, China, where he is a professor in the School of Automation. He was a visiting scholar with the Department of Electrical Engineering, Tohoku University, Sendai, Japan, from 1989 to 1990, and a visiting research scholar with the Department of Control and Systems Engineering, Tokyo Institute of Technology, from 1996 to 1999. He was a visiting professor at the School of Mechanical, Materials, Manufacturing Engineering and Management, University of Nottingham, Nottingham, UK, from 2001 to 2002. His current research interests include process control, robust control, and intelligent systems.

Prof. Wu is a Fellow of the IEEE and a Fellow of the Chinese Association of Automation. He received the IFAC Control Engineering Practice Prize Paper Award in 1999 (together with M. Nakano and J. She).